Available online at www.sciencedirect.com

SCIENCE DIRECT®

PERGAMON

International Journal of Multiphase Flow 29 (2003) 1117–1135

International Journal of Multiphase Flow

www.elsevier.com/locate/ijmulflow

Thermocapillary interaction of two bubbles or drops

S. Nas [a,*], G. Tryggvason [b]

[a] *Department of Aeronautical and Astronautical Engineering, Istanbul Technical University, Maslak, 34469 Istanbul, Turkey*

[b] *Department of Mechanical Engineering, Worcester Polytechnic Institute, Worcester, MA 01609-2280, USA*

Received 25 October 2000; received in revised form 13 April 2003

Abstract

Numerical simulations of the thermocapillary motion of a pair of two- and three-dimensional fully deformable bubbles and drops are presented. The Navier–Stokes equations coupled with the energy conservation equation are solved by a Front Tracking/Finite Difference Method. The material properties of the drop/bubble fluid and the ambient fluid are different, and surface tension depends on the temperature. At finite Reynolds (*Re*) and Marangoni (*Ma*) numbers, the results show that bubbles and light drops line up perpendicular to the temperature gradient, while spacing themselves evenly across the channel. This contrasts with the zero Reynolds and Marangoni previous results where the velocity of each bubble is unaffected by interactions between bubbles.

Keywords: Thermocapillary migration of bubbles/drops; Multiphase flow; Front-tracking finite-difference method

1. Introduction

Bubbles and drops suspended in a fluid with a temperature gradient will move toward the hot region due to thermocapillary forces. Surface tension generally decreases with increasing temperature and the non-uniform surface tension at the fluid interface leads to shear stresses that act on the outer fluid by viscous forces, thus inducing a motion of the fluid particle (a bubble or a drop) in the direction of the thermal gradient. In space, where buoyancy forces are negligible, thermocapillary forces can be dominant and can lead to both desirable and undesirable motion of fluid particles. Space-based containerless processing of materials such as glass is believed to have the potential of producing very pure materials (Uhlmann, 1982) and thermocapillary migration

* Corresponding author.
E-mail address: nas@itu.edu.tr (S. Nas).

0301-9322/03/$ - see front matter
doi:10.1016/S0301-9322(03)00084-3

may provide mechanisms to remove gas bubbles from the melt. Control of vapor bubbles forming in both the fuel systems of liquid-rockets (Ostrach, 1982) and the cooling system of space habitats may be achievable using thermocapillary migration. Thermocapillary migration may also lead to accumulation of gas bubbles on the hot surface of heat exchangers, therefore reducing their efficiency. In practical applications, it is frequently necessary to deal with a large number of bubbles or drops and their collective behavior may differ substantially from what one might expect based on results for a single particle.

Thermal migration of gas bubbles was first examined experimentally by Young et al. (1959) who found an analytical expression for the terminal velocity of a single spherical drop in the limit of negligible convective transport of momentum and energy. The migration velocity of a non-deformable gas bubble for small but non-zero convective heat transfer in the limit of zero Reynolds number was obtained by Subramanian (1981) using asymptotic expansion technique. Subramanian (1983) later extended this work to liquid drops. Balasubramaniam and Chai (1987) gave an exact solution for the migration velocity of a single drop in the limit of negligible convective transport of energy and Shankar and Subramanian (1988) found the thermocapillary migration of a spherical gas bubble in the limit of zero Reynolds number at values of the Marangoni number ranging from 0 to 200 using a finite difference method to solve the energy equation. Szymczyk and Siekmann (1988) computed the thermocapillary motion of a gas bubble accounting fully for the convective transport of energy and momentum but assuming a *non-deformable* bubble. This work was then extended by Balasubramaniam and Lavery (1989) who found the terminal velocity of an isolated non-deformable axisymmetric spherical bubble for a large range of the governing non-dimensional numbers. Both of these studies show that the scaled terminal velocity is a decreasing function of *Ma* at fixed *Re*, and an increasing function of *Re* at fixed *Ma*. Haj-Hariri et al. (1990) calculated analytically the correction of the thermocapillary velocity of a drop due to small inertial effects. The effect of surface deformation on the terminal velocity of a single bubble was investigated numerically by Chen and Lee (1992) who concluded that surface deformation considerably reduces the terminal velocity. Computational results for a gas bubble, similar to those of Balasubramaniam and Lavery have also been obtained by Treuner et al. (1996). Balasubramaniam and Subramanian (1996) found analytically that the thermocapillary migration velocity of a bubble approaches a non-zero asymptotic limit as the Marangoni number goes to infinity, regardless of the value of the Reynolds number. Haj-Hariri et al. (1997) found the migration velocity of an isolated drop for different governing parameters allowing deformation. Although their computations were three-dimensional, the steady drop shapes were always axisymmetric, being oblate or prolate depending on the density ratio. Welch (1998) reported the effect of non-dimensional numbers on the transient thermocapillary migration of a deformable bubble and concluded also that the deformation reduces the terminal velocity. For non-zero values of non-dimensional parameters, it was reported that the terminal velocity of the bubble decreases as the deformation increases. Ma et al. (1999) analyzed the thermocapillary motion of an non-deformable single drop, and concluded that the scaled migration velocity decreases with *Ma*, reaches a minimum, and then increases with *Ma* when *Ma* is large enough.

The behavior of a single fluid particle in a temperature gradient is reasonably well understood. The terminal velocity of a gas bubble in an unbounded domain decreases rapidly with increasing capillary number, increases very weakly with increasing Reynolds number, and decreases with increasing Marangoni number. On the other hand, the terminal velocity of a single drop first

decreases with increasing Marangoni number, attains a minimum and then increases with a further increase in the Marangoni number. The terminal velocity of a single bubble decreases with increasing capillary number (Ca) while drops deform oblate or prolate depending on density ratio. While considerable effort has been devoted to the study of the thermocapillary migration of a single fluid particle, only a few researchers have looked at the collective behavior of two or more particles. Meyyapan et al. (1983) investigated analytically the motion of two non-deformable bubbles, moving along their lines of center, and found that in the limit of zero Reynolds and Marangoni numbers each bubble moves with the velocity of an isolated single bubble. In the case of unequal sized bubbles, the smaller one always moves faster than a single isolated bubble of the same size and the larger one moves slightly slower than a single bubble. Meyyapan and Subramanian (1984) extended the analysis of Meyyapan et al. (1983) to the motion of two bubbles oriented arbitrarily with respect to the temperature gradient and showed that equal size bubbles move with the velocity of a single isolated bubble. This work was generalized to arbitrary number of equal size bubbles by Acrivos et al. (1990) who showed that each bubble moves completely independently of the other bubbles. This remarkable result is, however, restricted to zero Reynolds and Marangoni numbers. The motion of two liquid drops oriented arbitrarily with respect to a temperature gradient was examined analytically by Anderson (1985) in the zero Reynolds and Marangoni number limit. He found that the terminal velocity of each drop is affected by the viscosity, conductivity, size ratio, and the distance between drops. For the special case of equal size gas bubbles, he confirmed the finding of Meyyapan and Subramanian (1984). By using the two-drop solution, he also showed that the mean velocity of a droplet suspension is lower than for a single drop. Keh and Chen (1990) considered the axisymmetric thermocapillary motion of two spherical droplets moving along their line of centers in a creeping flow. They showed that two identical liquid droplets migrate faster than a single drop of the same size. For two gas bubbles with equal radii, there was no interaction for all separation distances in agreement with Meyyapan and Subramanian (1984). Later Keh and Chen (1992) investigated the axisymmetric migration of a chain of spherical drops and gas bubbles along their line of centers. In the case of multiple gas bubbles, it was demonstrated again that the migration velocity of each bubble is unaffected by the presence of the other bubbles, if the bubbles are of the same size. Wei and Subramanian (1993) investigated theoretically the quasi-static thermocapillary migration of a chain of two and three spherical bubbles for zero Marangoni and Reynolds numbers. Keh and Chen (1993) considered the migration of drops oriented arbitrarily with respect to the temperature gradient in the limit of zero Marangoni and Reynolds numbers. Unlike drops moving along their line of centers (examined by Keh and Chen (1990)), drops moving with their line of centers perpendicular to the temperature gradient migrate slower than a single drop. For early studies of the thermocapillary motion of a single bubble or drop, as well as a discussion of experimental studies the reader is referred to the review papers by Subramanian (1992) and by Wozniak et al. (1988).

The investigations of interactions of bubbles and drops discussed above have all been limited to zero Reynolds and Marangoni numbers. In this paper we present a computational study of the thermocapillary migration of two fully deformable bubbles and drops for non-zero values of the Reynolds and Marangoni numbers. A few preliminary results were reported in Nas and Tryggvason (1993) for two-dimensional fluid particles and the method is extended here for fully deformable three-dimensional fluid particles.

2. Formulation and numerical method

2.1. Governing equation

The physical problem and the computational domain are sketched in Fig. 1. The domain is periodic in the x-direction and bounded by rigid walls in the z-direction. The material properties of the fluid particle are denoted by the subscript i and the properties of the ambient fluid are denoted by the subscript 0. The top wall is hot and the bottom wall is cold, and initially the temperature varies linearly in the z-direction.

The Navier–Stokes questions are valid for both fluids, and a single set of equations can be written for the whole domain as long as the jump in viscosity and density is correctly accounted for and surface tension is included. The two-dimensional Navier–Stokes equations written in conservation form are

$$\frac{\partial \rho \mathbf{u}}{\partial t} + \nabla \cdot (\rho \mathbf{u}\mathbf{u}) = -\nabla p + \nabla \cdot \mu(\nabla \mathbf{u} + \nabla \mathbf{u}^T) + \int_B \delta(\mathbf{x} - \mathbf{x}_f) \frac{\partial}{\partial s}(\sigma \mathbf{t})\, \mathrm{d}s, \tag{1}$$

where the last term is the surface tension acting on the interface, included as a body force by representing it as a delta function. Here $\mathbf{u}$ is the velocity field, p is the pressure, ρ is the density, μ is the viscosity, σ is the surface tension, $\mathbf{t}$ is a unit tangent vector, s is the arc length along the interface, δ is a two or three-dimensional delta function, $\mathbf{x}_f$ is the position of the interface, and the integral is over the interface separating the fluids.

The energy equation is

$$\rho c_p \left(\frac{\partial T}{\partial t} + \nabla \cdot \mathbf{u} T \right) = \nabla \cdot (k \nabla T), \tag{2}$$

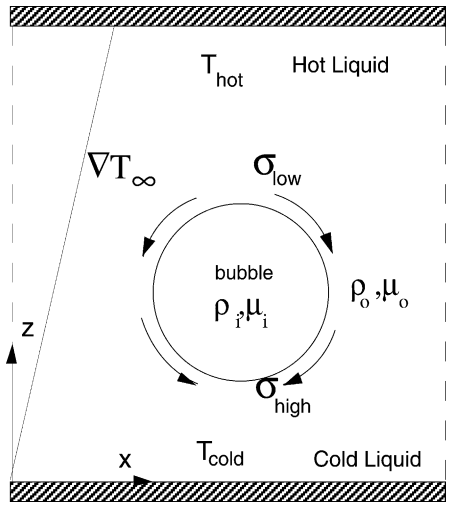

Fig. 1. The computational domain. The top and bottom walls are no-slip boundaries with constant temperature T_{hot} and T_{cold}, and the horizontal boundaries are periodic.

where T is the temperature and k and c_p are the coefficients of heat conduction and heat capacity, respectively, and heat generation is assumed to be negligible. Both fluids are immiscible and the material properties are constant in each fluid. The equations of state for density, viscosity, heat capacity, and heat conduction are therefore:

$$\frac{\mathrm{D}\rho}{\mathrm{D}t} = 0; \quad \frac{\mathrm{D}\mu}{\mathrm{D}t} = 0; \quad \frac{\mathrm{D}k}{\mathrm{D}t} = 0; \quad \frac{\mathrm{D}c_p}{\mathrm{D}t} = 0; \tag{3}$$

where $(\mathrm{D}/\mathrm{D}t) = (\partial/\partial t) + \mathbf{u}\cdot\nabla$ is the substantial derivative. The incompressibility constraint gives a solenoidal velocity field

$$\nabla\cdot\mathbf{u} = 0. \tag{4}$$

Combining the momentum equation and the incompressibility condition leads to a non-separable elliptic equation for the pressure.

The surface tension is taken to be a linearly decreasing function of the temperature,

$$\sigma = \sigma_0 + \sigma_T(T_0 - T), \tag{5}$$

where

$$\sigma_T = -\frac{\mathrm{d}\sigma}{\mathrm{d}T} = \text{constant} \tag{6}$$

and σ_0 is the surface tension at a reference temperature T_0. The coefficient σ_T is positive for most fluids and it, in general, depends on temperature. However, the assumption of a constant σ_T provides a good approximation in a range of small temperature variation.

The flow is governed by a, σ_0, μ_0, ρ_0, c_{p0}, k_0, μ_i, ρ_i, $c_{p\mathrm{i}}$, k_i, σ_T, and ∇T_∞ where a is the radius of the initially spherical fluid particle and ∇T_∞ is the temperature gradient in the ambient fluid far from the fluid particle. We first define a reference velocity $U_\mathrm{r} = (\sigma_T a/\mu_0)|\nabla T_\infty|$ and a reference time scale $t_\mathrm{r} = a/U_\mathrm{r}$, and then the governing non-dimensional numbers are given by

$$Ma = \frac{U_\mathrm{r} a}{\alpha_0}, \quad Re = \frac{U_\mathrm{r} a}{\nu_0}, \quad Ca = \frac{U_\mathrm{r}\mu_0}{\sigma_0}, \quad \rho^* = \frac{\rho_\mathrm{i}}{\rho_0}, \quad \mu^* = \frac{\mu_\mathrm{i}}{\mu_0}, \quad c_p^* = \frac{c_{p\mathrm{i}}}{c_{p0}}, \quad k^* = \frac{k_\mathrm{i}}{k_0}, \tag{7}$$

where $\alpha_0 = k_0/(\rho_0 c_{p0})$ and $\nu_0 = \mu_0/\rho_0$ are the thermal diffusivity and the kinematic viscosity of the ambient fluid, respectively. Ma is the Marangoni number, Re is the Reynolds number, and Ca is the capillary number. These three non-dimensional numbers are based on the properties of the ambient fluid. Sometimes the Prandtl number, $Pr_0 = \nu_0/\alpha_0$ is used instead of Re. In the limit of zero capillary, Reynolds, and Marangoni numbers, the terminal velocity of a single gas bubble in unbounded fluid is half of the reference velocity, U_r. While most analytical and numerical studies on thermocapillary motion have been confined to these limits, we do not make any such assumption here.

2.2. Numerical method

The numerical technique used for the simulations presented in this paper is the front tracking/finite difference method for multi-fluid flows developed by Unverdi and Tryggvason (1992a,b). To solve the Navier–Stokes equations we use a fixed, regular, staggered grid and discretize the momentum equations using a conservative, second-order central difference scheme for the spatial

variables and an explicit predictor–corrector, second-order projection time-integration scheme. The interface is represented by discrete computational points that are moved by the fluid velocity interpolated from the fixed grid. These points are connected to form a front that is used to keep the density and viscosity stratification sharp, and to calculate surface tension. The pressure equation is non-separable since the density varies and we used a multigrid package (MUDPACK from NCAR, Adams, 1989) to solve the pressure equation.

In order to compute the temperature dependent surface tension, the temperature on the front is interpolated from the fixed grid using the interpolation function described by Peskin (1977) and the surface tension calculated by Eq. (5). In two-dimensional simulations, the net force on each element is found directly by

$$\mathbf{F_s} = \oint_{\text{elem}} \frac{\partial}{\partial s}(\sigma \mathbf{t})\,\mathrm{d}s = (\sigma \mathbf{t})_2 - (\sigma \mathbf{t})_1, \tag{8}$$

where the unit tangent vector $\mathbf{t}$ is computed by fitting a Lagrange polynomial to the end-points of each element and the end points of the adjacent elements. For three-dimensional flow, the force is found by

$$\mathbf{F_s} = \oint_{\text{elem}} \sigma \mathbf{t} \times \mathbf{n}\,\mathrm{d}s. \tag{9}$$

Here $\mathbf{t}$ is a unit tangent vector along the edge of the triangular surface element, and $\mathbf{n}$ is a unit normal vector to the same surface element. By finding the force directly, we explicitly enforce that the integral over any portion of the surface gives the right value, and for closed surfaces, in particular, the integral of the surface tension over the whole surface is exactly zero. The surface forces acting on the interface are distributed to the neighboring fixed Eulerian grid points by the same distribution function used to interpolate the temperature. The velocity field is then advected using the pressure, viscous stresses and surface tension at each time step. The temperature field is advected in time using central differencing for the spatial derivatives and the same second-order time-stepping method used for the momentum equation. The numerical method has been implemented for two-dimensional (plane or axisymmetric) and three-dimensional geometries. The details of the present numerical method can be found in Tryggvason et al. (2001).

3. Results and discussion

For all the results presented here, uniform Cartesian grids are used. The computational domain and the boundary conditions are sketched in Fig. 1. In both two- and three-dimensional cases, the top and bottom boundaries are treated as no-slip walls and the temperature is fixed at the prescribed wall temperatures. In other directions, periodic boundary conditions are used for both the flow and temperature fields. Initially, the drops and bubbles are taken as infinitely long circular cylinders in two-dimensional cases and as spheres in three-dimensional cases. The fluid is initially at rest and the temperature linearly increases from the cold bottom wall toward the hot top wall.

3.1. Resolution test and validation

The method described above is first applied to several test cases in order to establish the accuracy of the numerical algorithm. To check the sensitivity of the results to grid refinement, the migration of a two-dimensional light drop is computed until it reaches a steady-state for two sets of the governing parameters. For the first case the non-dimensional numbers are chosen as $Re = 2.5 \times 10^{-3}$, $Ma = 2.5 \times 10^{-3}$ and $Ca = 10^{-3}$, and the ratios of the material properties of the drop to that of the ambient fluid are all set equal to 0.5. The computational domain is a square extending four drop radii in each direction and we use grids with 32×32, 64×64 and 128×128 points. This corresponds to 16, 32, and 64 grid points per drop, respectively. Fig. 2 shows the migration velocity of the drop versus time for these three cases. Note that, in all the results presented in the paper, the migration velocity is simply taken as the drop velocity in z-direction (denoted by V) since the other components of the drop velocity are about an order of magnitude smaller then V, and it is non-dimensionalized by the reference velocity, i.e., $V^* = V/U_r$. As the grid resolution is increased, the terminal velocities converge and the difference in terminal velocities calculated with 64×64 and 128×128 grids is below 2%. For the second test case, the non-dimensional parameters are chosen as $Re = 5$, $Ma = 20$, and $Ca = 0.01666$, the material property ratios are set to 0.5, and the computational domain is a rectangle of size 4×8 drop radii. Fig. 3 shows the migration velocity of the drop versus time, computed using 32×64, 64×128 and 128×256 grid points. The terminal velocities converge as the resolution is increased, and the difference between the results on the finest grids is very small (about 0.6%). The difference in the terminal velocities computed with 16 and 32 grid points per drop diameter resolution is about 2.1%. Therefore, the 32 grid points per drop/bubble diameter resolution is chosen for most of the simulations presented here in order to save computational resources. Where only qualitative

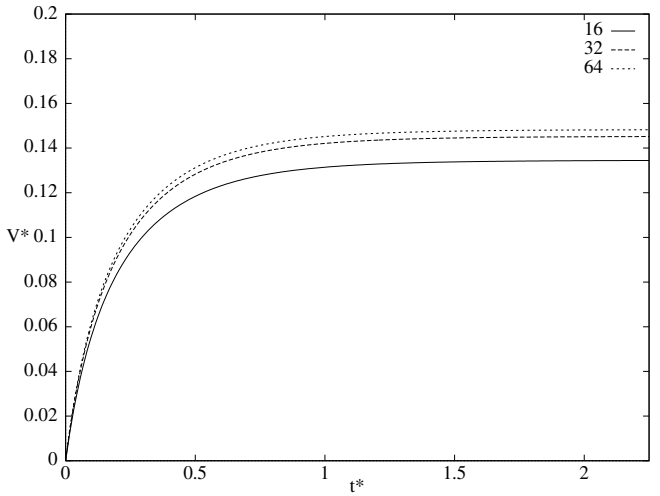

Fig. 2. Resolution test for a single two-dimensional drop in a computational domain with 4 drop radii in each coordinate direction. The migration velocity of the drop is plotted versus time for three grid resolutions corresponding to 16 (—), 32 (- - -) and 64 (···) grid points per drop diameter, respectively. $Re = Ma = 2.5 \times 10^{-3}$, $Ca = 10^{-3}$, and the material property ratios are 0.5.

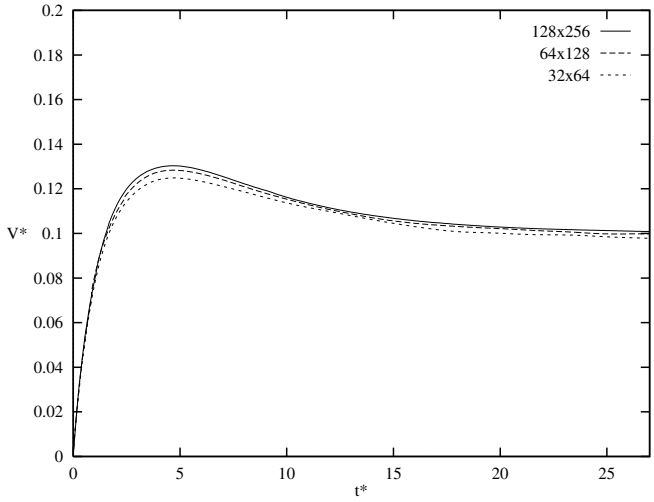

Fig. 3. Resolution test for a single two-dimensional drop in a computational domain with 4 drop radii in each coordinate direction. The migration velocity of the drop is plotted versus time for three grid resolutions corresponding to 16 (···), 32 (- - -) and 64 (—) grid points per drop diameter, respectively. $Re = 5$, $Ma = 20$, $Ca = 0.01666$, and the material property ratios are 0.5.

information is required, as few as 16 grid points per drop/bubble diameter can be used as the relative percentage error is approximately 3% compared to the finest grid computation.

To test the implementation of the code, we have compared the migration velocity of a fully three-dimensional drop to analytical results in the creeping flow limit. For zero Reynolds and Marangoni numbers, Young et al. (1959) found that the scaled terminal velocity of a spherical drop is

$$V_{\mathrm{YGB}} = \frac{2}{(2+k^*)(2+3\mu^*)}. \tag{10}$$

Here k^* is the ratio of the heat conductivity of the drop to that of the ambient fluid and μ^* is the ratio of the viscosities. For a gas bubble, this formula reduces to $V_{\mathrm{YGB}} = 0.5$ in the limit of zero conductivity and viscosity ratios. In Fig. 4, the terminal migration velocity of a drop with $Re = 2.5 \times 10^{-3}$, $Ma = 2.5 \times 10^{-3}$, $Ca = 10^{-3}$, and $k^* = \mu^* = 0.5$ is plotted versus the scaled distance $H = h/a$ where h is the distance between the wall and the drop centroid. For these property ratios Eq. (10) gives $V_{\mathrm{YGB}} = 0.228$ for the creeping flow limit (dashed horizontal line). In all cases the drop is resolved by about 32 grid points per diameter. The wall effects are reduced as the computational domain is increased while keeping the number of the grid points per drop diameter the same, the numerical results approach the analytical solution for a non-deformable drop in an unbounded domain. The convergence is shown in Fig. 4.

3.2. Two-dimensional studies of two bubbles

The interaction of two fluid particles is generally a fully three-dimensional problem, although the in-line interaction of particles can be examined in an axisymmetric geometry. Since fully three-

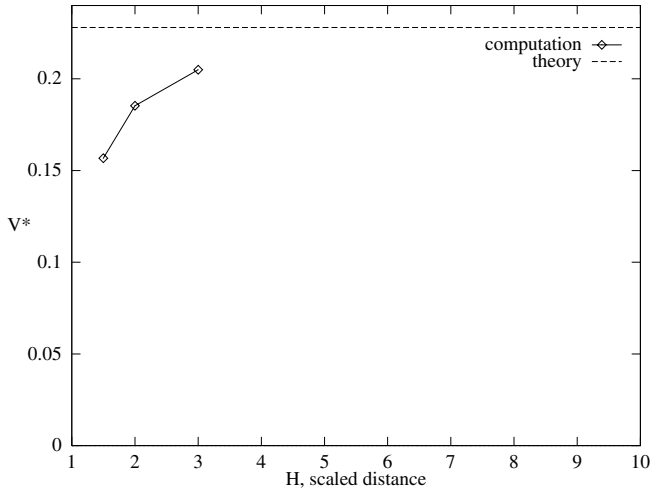

Fig. 4. The steady-state migration velocity of a three-dimensional drop versus the scaled distance. The computational domains corresponding to the scaled distance $H = 1.5$, 2.0, and 3.0 are resolved by 48^3, 64^3 and $80^2 \times 96$ grid points, respectively. The drop is resolved by 32 grid points per drop diameter in all three cases.

dimensional computations are fairly expensive, we have done a number of two-dimensional simulations to develop insight into how the particles interact and how the interactions depend on the governing parameters. These simulations do not give results that can be expected to be in quantitative agreement with experiments, but as three-dimensional simulations presented later in the paper demonstrate, the qualitative behavior is well predicted.

First, we explore the motion of gas bubbles where the material properties of the fluid particle are small compared to the ambient fluid. We choose the ratio of material properties to be 1/25. Further reduction does not change the results in any significant way, but the required computational time increases. The other governing parameters are $Re = Ma = 40$ and $Ca = 0.041666$. The computational domain is 8×16 bubble radii and the resolution is 128×256 grid points. The bubble on the left is initially at $(x/a, z/a) = (2.9, 4.0)$, and the one on the right is at $(x/a, z/a) = (5.1, 5.8)$. Fig. 5 shows the results at four different times. The top row shows the bubbles and the isotherms and the bottom row shows the bubbles and streamlines in a frame of reference moving with the bubble on the right. As the bubbles start to move, hot fluid is drawn down between the bubbles, increasing the temperature difference across the left bubble and reducing the temperature difference across the right bubble. The bubble on the left therefore catches up with the bubble on the right and moves slightly ahead. As it does so, the high velocity between the bubbles draws hot fluid in between them and the bubbles move toward each other. Eventually the bubbles touch and although the bubbles are not allowed to coalesce, they do block any flow of ambient fluid between them. Hotter fluid therefore flows around the pair and the bubbles move away from each other. Both bubbles drift to the right and in the third frame the bubble initially on the right moves across the periodic vertical boundaries. The bubble coming from the left initially moves toward the other bubble, but in the last frame, when the bubbles are just about to hit the top wall, they move away from each other.

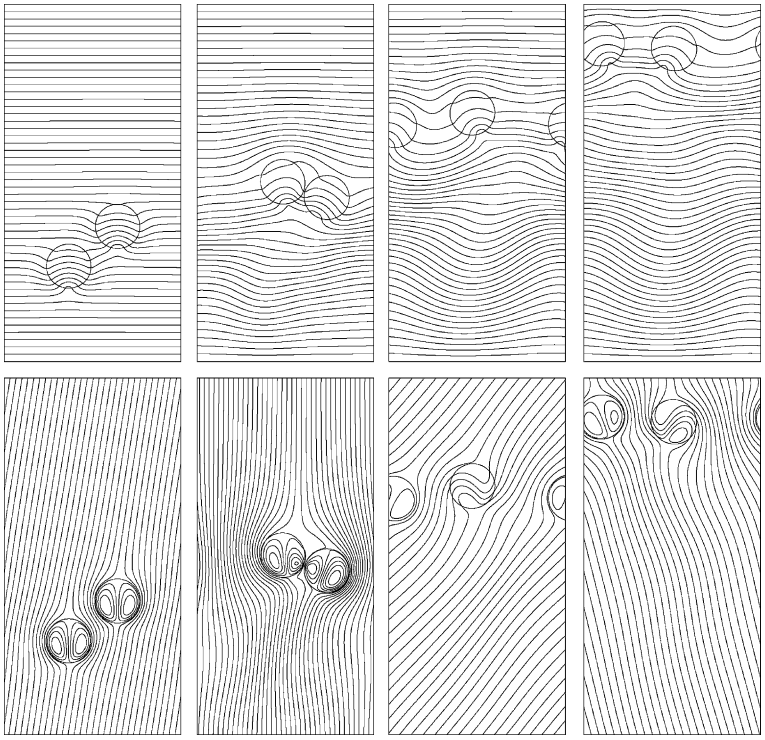

Fig. 5. Isotherms (top) and streamlines (bottom) for selected frames from the computation of two bubble interaction. 50 equally spaced isotherms and 40 streamlines, in a frame of reference moving with the bubble on the right, are shown. Time progresses from left to right. The non-dimensional times, t^* are 3.8, 25.3, 69.5 and 107.5, and $Re = Ma = 40$, $Ca = 0.04166$, and material property ratios are 1/25.

The scaled migration velocity of each bubble versus the non-dimensional time is plotted in Fig. 6(a). In this figure, the dotted line labeled by "centroid" refers to the scaled migration velocity of the center of mass of the bubble system. After the bubbles start to interact, the bubble on the left is accelerated, but the bubble on the right is slowed down. Indeed, the bubble on the right moves away from the hot wall for a short period. The velocities are then approximately equal, although the bubble initially on the right moves slightly faster as it catches up again with the other bubble. The vertical separation of the bubbles is plotted versus their horizontal separation in Fig. 6(b). The bubbles first move straight toward the hot wall. After the bubble initially on the left has moved slightly ahead of the bubble on the right, they start to move apart. Since the bubbles hit the top wall, they have not reached a steady-state motion when the simulation is stopped, but one can speculate that they would eventually move side by side, evenly spaced across the computational domain.

We have repeated these computations for various Reynolds and Marangoni numbers to examine the effects of these numbers on the migration of the bubbles. In Fig. 7, the vertical separation is plotted versus the horizontal separation for the same initial bubble location as in Fig. 5. The bubble initially further away from the hot wall moves faster in all cases and overtakes the other bubble. The bubbles then drift apart, except in the $Re = Ma = 10$ case where they move together. With the exception of low Re and Ma case, the results are very similar to the

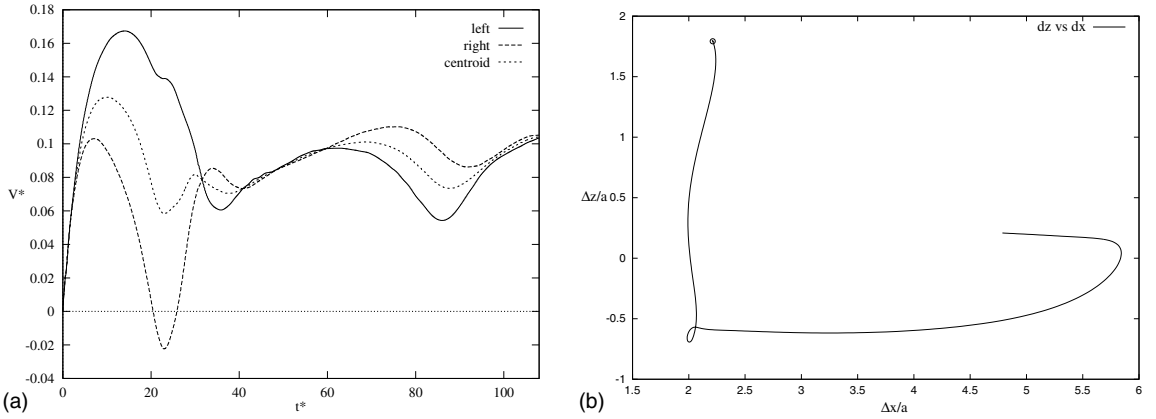

Fig. 6. (a) Migration velocity versus time. The solid, dashed and dotted lines denote the migration velocities of the left bubble, the right bubble and the center of mass of the bubble system. (b) Vertical versus horizontal separation of the bubbles. The bubble system is the same as in Fig. 5 and the small circle indicates the initial separation of the bubbles.

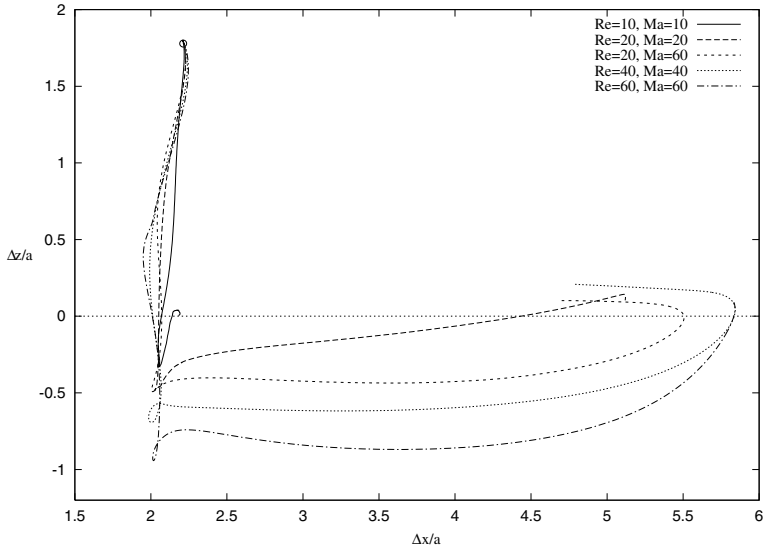

Fig. 7. Vertical separation versus horizontal separation of bubbles computed using several *Re* and *Ma* numbers. Other parameters are the same as in Figs. 5 and 6. The small circle indicates the initial separation of the bubbles.

$Re = Ma = 40$ case. This suggests that the tendency of bubbles to line up approximately evenly spaced, perpendicular to the temperature gradient is not very sensitive to the exact value of the governing parameters.

3.3. Light drops

Next, we examine a fluid pair where the material properties of the light drop are half of those of the ambient fluid. All other parameters are the same as in the simulation shown in Fig. 5. Fig. 8

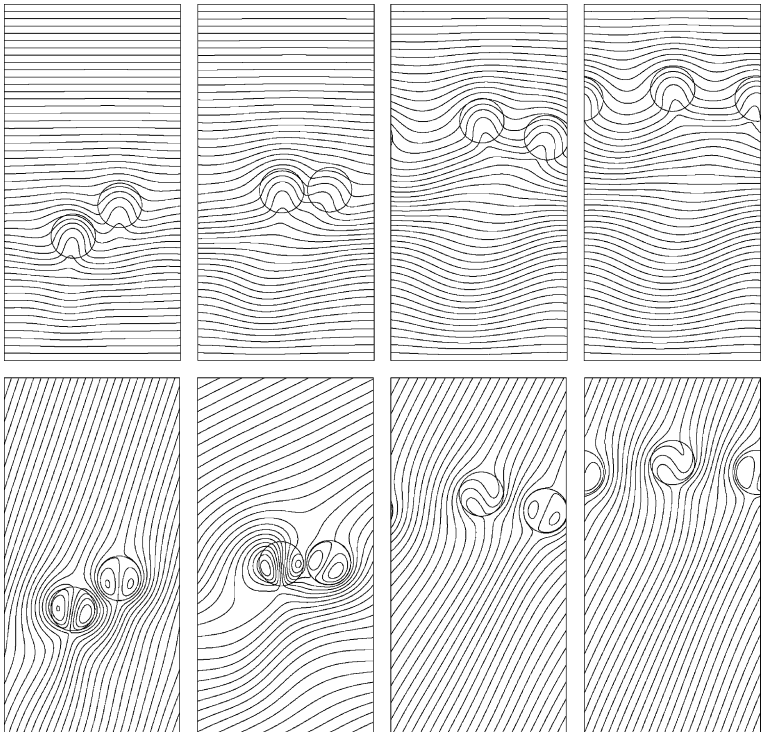

Fig. 8. Isotherms (top) and streamlines (bottom) for selected frames from the computation of two drop interaction. 50 equally spaced isotherms and 40 streamlines, in a frame of reference moving with the drop on the right, are shown. Time progresses from left to right. The non-dimensional times, t^* are 20, 40, 80, and 100. $Re = Ma = 40$, $Ca = 0.04166$, and material property ratios are 0.5.

shows the drops and the isotherms (top row) and the streamlines with respect to a frame moving with the drop on the right (bottom row) at four different times. The evolution for this case is similar to what is seen for the bubbles in the previous section: The temperature change across the drop on the left is increased and the change across the right drop is decreased as the left drop catches up with the drop on the right. After the drops first move toward each other, they then separate since no fluid can flow between them. The drops then migrate side by side, almost equispaced across the channel. The final equilibrium configuration can be explained by the fact that once the drops are side by side and moving toward hot wall, the ambient fluid has to flow down between them to satisfy continuity and when the spacing between the drops is uneven there is greater flow through the larger spacing. Since the downward moving fluid is hotter, the isotherms are pushed farther down in the large space than in the small space. Since the drops move from colder regions to hotter ones, this leads to a lateral motion (in addition to the motion toward the hot wall) where the small space becomes larger and the large space becomes smaller until the drops have arranged themselves in a horizontal array with equal spaces between them. Fig. 9 shows the migration velocity (a) and the vertical separation of the drops versus horizontal separation (b) for the case in Fig. 8. This plot shows that the drop on the left migrates at an almost steady state velocity after the drops are about half way toward the hot wall.

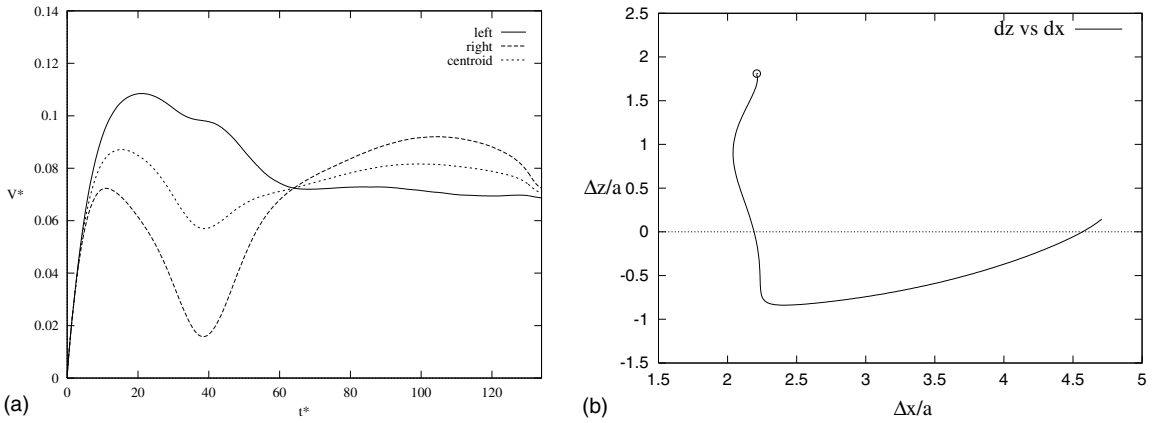

Fig. 9. (a) Migration velocity of the drops in Fig. 8 versus time. The solid, dashed and dotted lines denote the migration velocities of the left drop, the right drop and the center of mass of the drop system. (b) Vertical versus horizontal separation distance. The small circle indicates the initial separation of the drops.

Results for different *Re* and *Ma* numbers shown in Fig. 10 where the vertical separation is plotted versus the horizontal separation exhibit similar behavior as seen in Fig. 9 and in all cases the drops close the vertical gap between them. As the Reynolds and Marangoni numbers increase, the interaction becomes stronger and the drops overshoot both the vertical and horizontal equilibrium separation. Since the drops hit the top wall, the transients have not been completely damped when the computations are terminated. The results suggest, however, that the drops will eventually line up evenly spaced perpendicular to the temperature gradient.

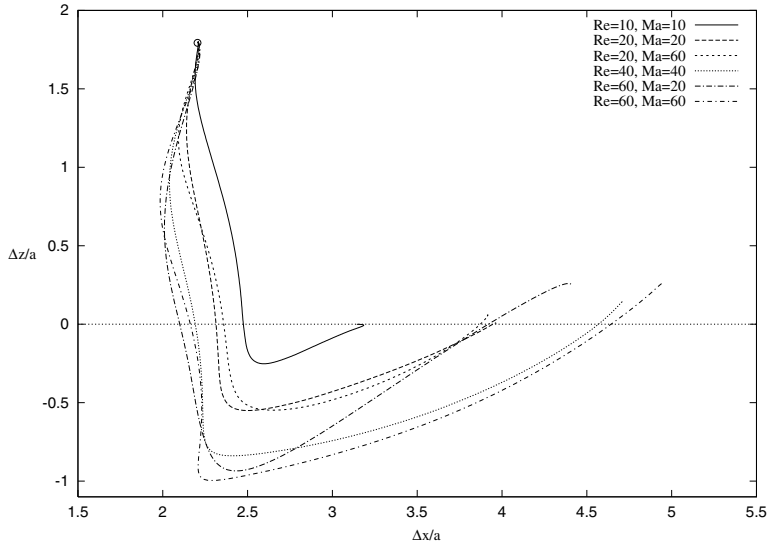

Fig. 10. Vertical separation versus horizontal separation of drops computed using several *Re* and *Ma* numbers. Other parameters are the same as in Figs. 8 and 9. The small circle indicates the initial separation of the drops.

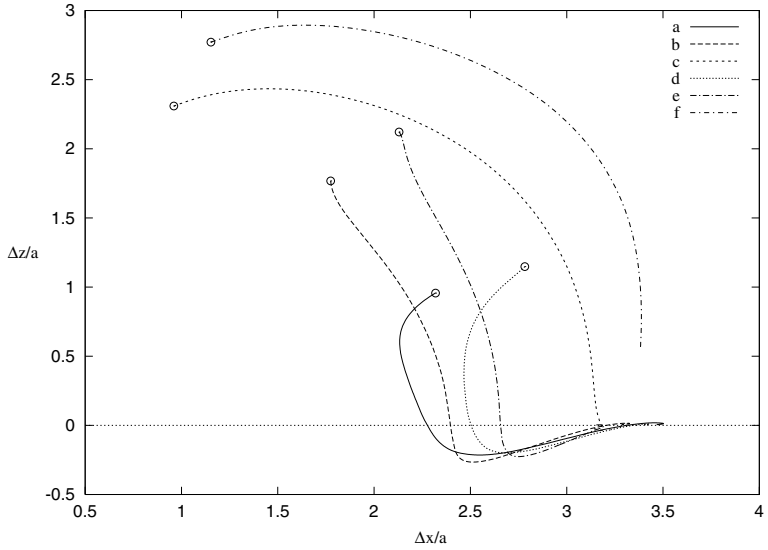

Fig. 11. The vertical separation versus the horizontal separation between two drops for several different initial locations. $Re = Ma = 10$, $Ca = 0.0141666$ and the material property ratios are 0.5. The small circles indicate the initial separation of the drops.

The effect of the initial orientation of the drops on their motion is also investigated by varying the gap between the drops and their angular position with respect to the initial temperature gradient. These cases are identified with the letters (a)–(f) in Fig. 11 where the vertical separation of the drops is shown versus the horizontal separation. The angle between the horizontal axis and a line connecting the centers of the drops is $\pi/8$ for (a) and (d), $\pi/4$ for (b) and (e), and $3\pi/8$ for (c) and (f). The middle point of the line connecting the centers of the drops is at $(x/a, z/a) = (1, 1)$. For cases (a)–(c), the gap between the drops, center to center, is 2.5 times the drop radius and for (d)–(f), this distance is three drop radii. The computations are performed in a domain which is 8×16 drop radii, resolved by 128×256 grid points. The non-dimensional numbers are $Re = 10$, $Ma = 10$ and $Ca = 0.041666$, and the material property ratios are equal to 0.5. As can be seen in the cases (a), (b), (d) and (e), the drops that are initially well separated horizontally quickly close the vertical gap and then drift apart. The drops in the cases (c) and (f), however, are initially placed closely together in the horizontal direction and must therefore first move to the side, before closing the vertical gap. In these cases the drops hit the top wall before the initial transient is completed.

3.4. Simulations of two three-dimensional light drops

While the two-dimensional simulations reported in Sections 3.2 and 3.3 give considerable insight into the interactions of two bubbles and light drops in thermocapillary motion, they do not yield results that can be compared directly with experimental observations. Since the velocity disturbance decays much slower in two-dimensions than in three dimensions, the two-dimensional computations are likely to over-predict the strength of the interactions. To examine how the

results change when the full three-dimensionality of the fluid particles is taken into account, some three-dimensional simulations are performed. For all the cases considered, the capillary number $Ca = 0.04166$ and the ratio of material properties of the light drop to the properties of the ambient fluid is set to 0.5. The computational resolution is $64 \times 32 \times 128$ grid points for a computational domain with dimensions $x/a = 5.71$, $y/a = 2.86$, and $z/a = 11.43$. Fig. 12 shows the drops along with the velocity and temperature in the middle cross-sectional plane at four different times for two simulations: (a) $Re = 20$ and $Ma = 60$; (b) $Re = 60$ and $Ma = 20$. For cases (a) and (b), the initial locations of the left and right drops are at $(x/a, z/a) = (1.71, 2.85)$ and $(x/a, z/a) = (2.14, 2.0)$, and $(x/a, z/a) = (2.14, 2.0)$ and $(x/a, z/a) = (3.57, 3.85)$, respectively. For

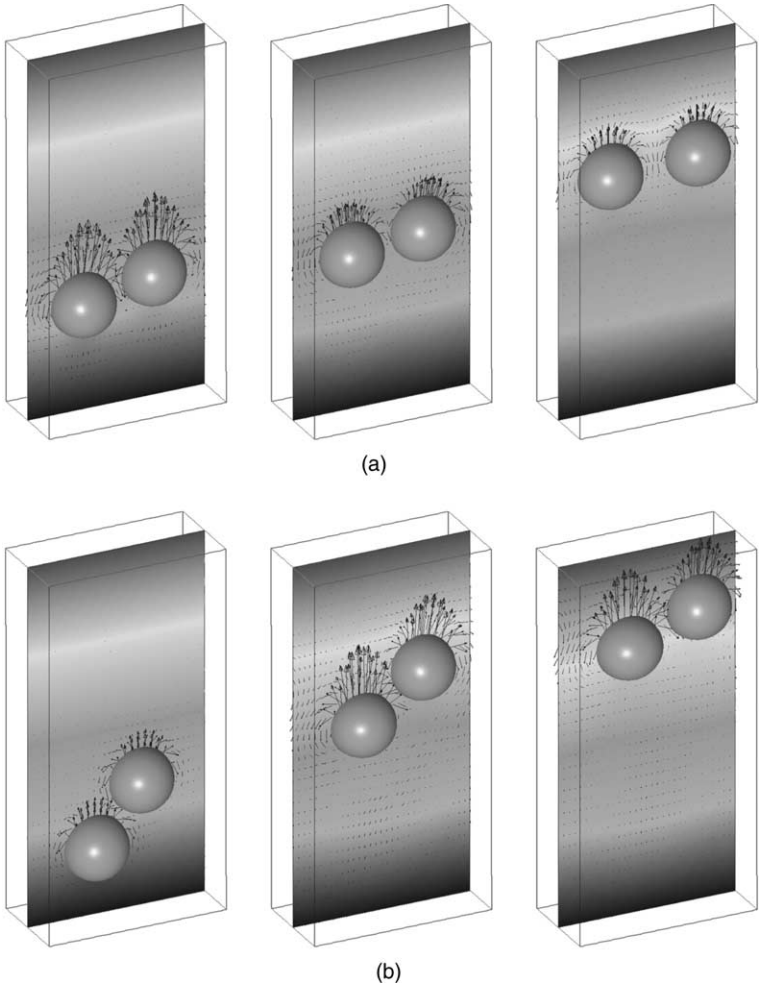

Fig. 12. Velocity and temperature fields for selected frames from fully three-dimensional simulation of the migration of two drops. The velocity field is shown at every other grid point in a plane through the middle of the computational domain. Time progresses from left to right. (a) Top row: t^* are 5.71, 22.85 and 57.14, and $Re = 20$, $Ma = 60$; (b) Bottom row: t^* are 3.5, 35.0 and 52.5, and $Re = 60$, $Ma = 20$. For both cases, $Ca = 0.04166$ and the computational domain is $(x/a, y/a, z/a) = (5.17, 2.86, 11.43)$.

both cases, the drops are located in the middle cross-sectional plane at $y/a = 1.43$. In order to show how the motion of the drops affects the temperature field, the drop contours and the isotherms in the middle cross-sectional plane are shown in Fig. 13 at the same times as in Fig. 12.

Initially, the light drops in Fig. 12(a) move rapidly toward the hot wall (top row), but then they slow down and drift apart. They also become more horizontally aligned. However, since the initial vertical separation was small, this motion is not very visible in Fig. 12(a). Fig. 13(a) shows that heat conduction is slow compared to the time scale of the motion, so cold fluid is carried with the drops toward the hot wall. The drops in Fig. 12(b) do not show the initially large velocity seen for the drops in Fig. 12(a), but the reduction in vertical separation of the drops is much clearer here. Since the Marangoni number is lower for the drops in Fig. 12(b) than in Fig. 12(a), the heat conduction is high in case (b). Fig. 13(b) shows that the fluid in the drops is only slightly colder than the surrounding fluid.

The velocity of the drops toward the hot wall is plotted versus time in Fig. 14. The velocities of drops in Fig. 12(a) and (b) are shown in Fig. 14(a) and (b), respectively. The large initial velocity of the drops in Fig. 12(a) is clearly visible in this plot and it is also clear that the drop on the left,

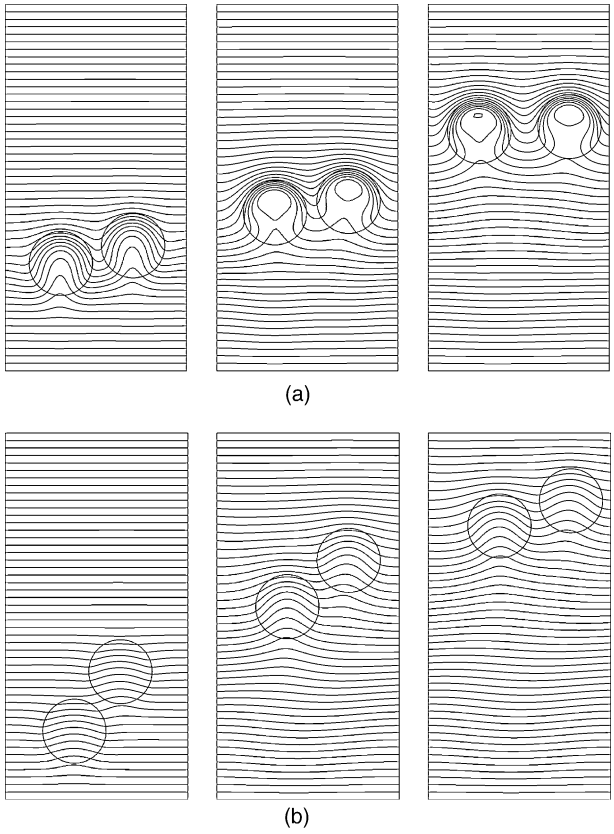

Fig. 13. Isotherms for selected frames from fully three-dimensional computation of migration of two drops. Time progresses from left to right. (a) Top row: t^* are 5.71, 22.85 and 57.14, and $Re = 20$, $Ma = 60$; (b) Bottom row: t^* are 3.5, 35.0 and 52.5, and $Re = 60$, $Ma = 20$. For both cases, $Ca = 0.04166$ and the computational domain is $(x/a, y/a, z/a) = (5.17, 2.86, 11.43)$.

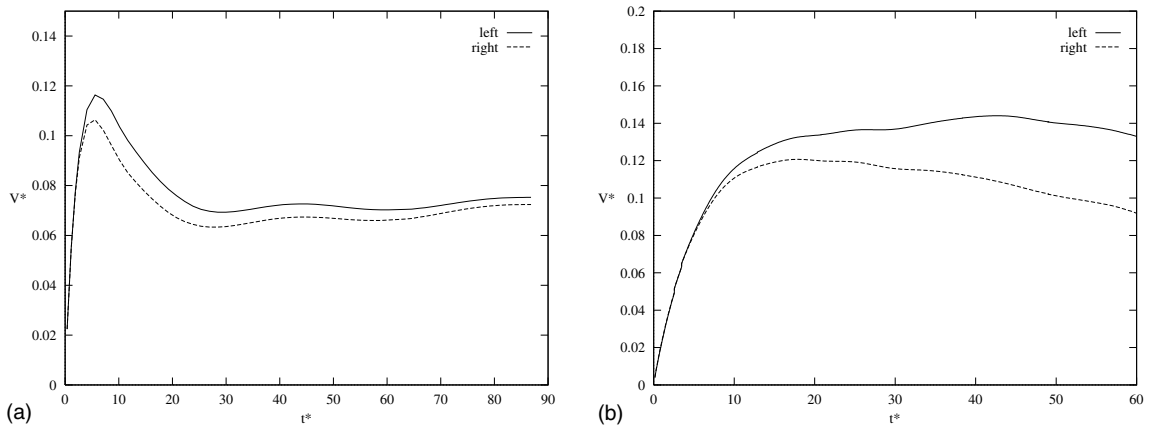

Fig. 14. Migration velocity of the drops in Fig. 12(a) and (b) versus time. (a) $Re = 20$, $Ma = 60$; (b) $Re = 60$, $Ma = 20$.

which was initially behind the drop on the right, has a slightly larger velocity. Near the end of the simulation, where the drops are oriented nearly horizontally with respect to each other, the difference in the velocities is reduced. The velocities of the drops in Fig. 12(b) evolve differently. There is no initial over-shoot and while the velocity of the left drop (initially behind) is larger, the difference continues to increase. It is therefore likely that the left drop will eventually overtake the right one and pass it.

In Fig. 15, the horizontal separation of the drops in Fig. 12, as well as for drops from a few other three-dimensional simulations, is plotted versus the vertical separation. The horizontal separation increases and the vertical separation decreases in all cases. Three simulations are

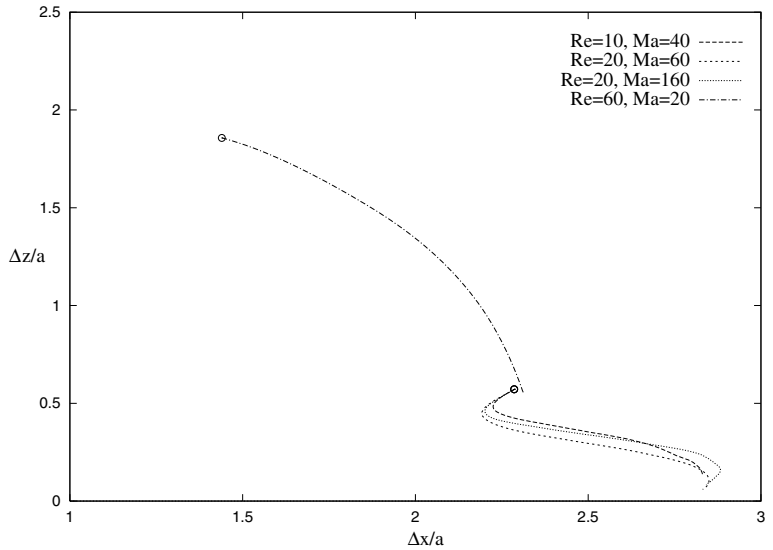

Fig. 15. The scaled vertical separation versus the horizontal separation of two drops for several *Re* and *Ma* numbers and two different initial conditions.The small circles indicate the initial separation of the drops.

started with a small vertical separation of the drops and all follow essentially the same path: First there is a slight increase in the vertical separation and then a nearly monotonic approach to an equilibrium position where the vertical separation is zero and the horizontal separation is about half the x-dimension of the computational domain, except for the case of $Ma = 160$ where drops slightly overshoot. The physical parameters of the three-dimensional results correspond to the two-dimensional simulations in Section 3.2, except that the initial locations of the drops are slightly different. In the two-dimensional simulations, if the initial horizontal separation is larger than about one drop radius, the vertical separation decreases. This is similar to the three-dimensional results, except that the two-dimensional vertical separation overshoots slightly and the eventual separation is at about 3.5 drop radii. In the fourth case, where $Re = 60$, the drops were initially placed with a large vertical and a small horizontal separations. Therefore, the drop that is initially behind must first move horizontally before it can catch up with the drop ahead. This behavior is also seen in the two-dimensional results.

4. Conclusions

The thermocapillary migration of two fluid particles toward a hot wall has been examined for non-zero values of the Reynolds and Marangoni numbers by numerical simulations and it is found that the particles interact strongly. Although the fluid particles are allowed to deform, it is observed that the light drop/bubble shapes change very little in all the cases considered here. The particle initially closer to the cold wall moves faster than the particle initially closer to the hot wall and in all cases it is found that the initially colder particle catches up with the hotter one. In some cases it is clear that the fluid particles eventually line up perpendicular to the temperature gradient and are evenly spaced. The strong interaction between fluid particles observed here contrast strongly with the behavior of bubbles for zero Reynolds and Marangoni numbers, where there is no interaction.

Acknowledgements

This study is funded by NASA grants NAG3-1317 and NAG3-2145. Some of the computations have been done at the NASA Goddard Research Center and the Center for Parallel Computing at the University of Michigan. We thank Drs. D. Jacqmin and R. Balasubramaniam at NASA Glenn Research Center for valuable discussions.

References

Acrivos, A., Jeffrey, D.J., Saville, D.A., 1990. Particle migration in suspensions by thermocappilary or electrophoretic motion. J. Fluid Mech. 212, 95–110.

Adams, J., 1989. MUDPACK: Multigrid fortran software for the efficient solution of linear elliptic partial differential equations. Appl. Math. Comput. 34, 113–146.

Anderson, J.L., 1985. Droplet interaction in thermocapillary motion. Int. J. Multiphase Flow 11, 813–824.

Balasubramaniam, R., Chai, A., 1987. Thermocapillary migration of droplets: An exact solution for small Marangoni numbers. J. Colloid Interface Sci. 119, 531–538.

Balasubramaniam, R., Lavery, J.E., 1989. Numerical simulation of thermocapillary bubble migration under microgravity for large Reynolds and Marangoni numbers. Num. Heat Transfer A 16, 175–187.

Balasubramaniam, R., Subramanian, R.S., 1996. Thermocapillary bubbles migration-thermal boundary layers for large Marangoni numbers. Int. J. Multiphase Flow 22, 593–612.

Chen, J.C., Lee, Y.T., 1992. Effect of surface deformation on thermocapillary bubble migration. AIAA J. 30, 993–998.

Haj-Hariri, H., Nadim, A., Borhan, A., 1990. Effect of inertia on the thermocapillary velocity of a drop. J. Colloid Interface Sci. 140, 277–286.

Haj-Hariri, H., Shi, Q., Borhan, A., 1997. Thermocapillary motion of deformable drops at finite Reynolds and Marangoni numbers. Phys. Fluids 9, 845–855.

Keh, H.J., Chen, S.H., 1990. The axisymmetric thermocapillary motion of two droplets. Int. J. Multiphase Flow 16, 515–527.

Keh, H.J., Chen, S.H., 1992. Droplet interactions in axisymmetric thermocapillary motion. J. Colloid Interface Sci. 151, 1–16.

Keh, H.J., Chen, S.H., 1993. Droplet interactions in thermocapillary migration. Chem. Eng. Sci. 48, 3565–3582.

Ma, X.J., Balasubramaniam, R., Subramanian, R.S., 1999. Numerical simulation of thermocapillary drop motion with internal circulation. Numer. Heat Transfer A-Appl. 35, 291–309.

Meyyapan, M., Subramanian, R.S., 1984. The thermocapillary motion of two bubbles oriented arbitrarily relative to a thermal gradient. J. Colloid Interface Sci. 197, 291–294.

Meyyapan, M., Wilcox, W.R., Subramanian, R.S., 1983. The slow axisymmetric motion of two bubbles in a thermal gradient. J. Colloid Interface Sci. 94, 243–250.

Nas, S., Tryggvason, G., 1993. Computational investigation of the thermal migration of bubbles and drops. AMD 174/FED 175 fluid mechanics phenomena in microgravity. In: Siniger, D.A., Thamson, R.L., Trefethen, L.M. (Eds.), ASME Winter Annual Meeting, pp.71–83.

Ostrach, S., 1982. Low gravity fluid flows. Ann. Rev. Fluid Mech. 14, 313–345.

Peskin, C.S., 1977. Numerical analysis of blood flow in the heart. J. Comput. Phys. 25, 220–252.

Shankar, N., Subramanian, R.S., 1988. The stokes motion of a gas bubble due to interfacial tension gradients at low to moderate Marangoni numbers. J. Colloid Interface Sci. 123, 512–522.

Subramanian, R.S., 1981. Slow migration of a gas bubble in a thermal gradient. AIChE J. 27, 646–654.

Subramanian, R.S., 1983. Thermocapillary migration of bubbles and droplets. Adv. Space Res. 3, 145–150.

Subramanian, R.S., 1992. The motion of bubbles and drops in reduced gravity. In: Chabra, R.P., De Kee, D. (Eds.), Transport Processes in Bubbles, Drops and Particles. Hemisphere Publishing Corp, Washington, DC, USA, pp. 1–42.

Szymczyk, J.A., Siekmann, J., 1988. Numerical calculation of the thermocapillary motion of a bubble under microgravity. Chem. Eng. Commun. 69, 129–147.

Treuner, M., Galdino, V., Gerberth, G., Langbein, D., Rath, H.J., 1996. Thermocapillary bubble migration at high Reynolds and Marangoni numbers under low gravity. J. Colloid Interface Sci. 179, 114–127.

Tryggvason, G., Bunner, B., Esmaeeli, A., Juric, D., Al-Rawahi, N., Tauber, W., Han, J., Nas, S., Jan, Y.-J., 2001. A front-tracking method for computations of multiphase flow. J. Comput. Phys. 169, 708–759.

Uhlmann, D.R., 1982. Glass processing in a microgravity environment. In: Rindone, G.E. (Ed.), Materials Processing in the Reduced Gravity Environment of Space. Elsevier, New York, USA, pp. 269–278.

Unverdi, S.O., Tryggvason, G., 1992a. A front-tracking method for viscous incompressible flows. J. Comput. Phys. 100, 25–37.

Unverdi, S.O., Tryggvason, G., 1992b. Computations of multi-fluid flows. Phys. D 60, 70–83.

Wei, H., Subramanian, R.S., 1993. Thermocapillary migration of a small chain of bubbles. Phys. Fluids A 5, 512–522.

Welch, S.W.J., 1998. Transient thermocapillary migration of deformable bubbles. J. Colloid Interface Sci. 208, 500–508.

Wozniak, G., Siekmann, J., Srulijes, J., 1988. Thermocapillary bubble and drop dynamics under reduced gravity-survey and prospects. Z. Flugwiss. Weltraumforsch. 12, 137–144.

Young, N.O., Goldstein, J.S., Block, M.J., 1959. The motion of bubbles in a vertical temperature gradient. J. Fluid Mech. 6, 350–356.